

1 **Statistically Steady State Large-Eddy Simulations**
2 **Forced by an Idealized GCM: 1. Forcing Framework**
3 **and Simulation Characteristics**

4 **Zhaoyi Shen¹, Kyle G. Pressel², Zhihong Tan^{3*}, Tapio Schneider^{1,4}**

5 ¹California Institute of Technology, Pasadena, California, USA.

6 ²Pacific Northwest National Laboratory, Richland, Washington, USA.

7 ³Department of the Geophysical Sciences, University of Chicago, Chicago, Illinois, USA.

8 ⁴Jet Propulsion Laboratory, Pasadena, California, USA.

9 **Key Points:**

- 10 • A framework in which LES is driven by large-scale forcing from a GCM is devel-
11 oped
12 • LES with large-scale forcing reaches steady states without nudging to reference
13 GCM profiles
14 • LES driven by the GCM is used to simulate different tropical cloud regimes across
15 the Walker circulation

*Princeton University, Princeton, New Jersey, USA.

Corresponding author: Zhaoyi Shen, zhaoyi@caltech.edu

Abstract

Using large-eddy simulations (LES) systematically has the potential to inform parameterizations of subgrid-scale (SGS) processes in general circulation models (GCMs), such as turbulence, convection, and clouds. Here we show how LES can be run to simulate grid columns of GCMs to generate LES across a cross-section of dynamical regimes. The LES setup approximately replicates the thermodynamic and water budgets in GCM grid columns. Resolved horizontal and vertical transports of heat and water and large-scale pressure gradients from the GCM are prescribed as forcing in the LES. The LES are forced with prescribed surface temperatures, but free-tropospheric temperature and moisture are free to adjust, reducing the imprinting of GCM fields on the LES. In both the GCM and LES, radiative transfer is treated in a unified but idealized manner (semi-gray atmosphere without water vapor feedback or cloud radiative effects). We show that the LES in this setup reaches statistically steady states without nudging to GCM profiles. The steady states provide training data for developing GCM parameterizations. The same LES setup also provides a good basis for studying the cloud response to global warming.

Plain Language Summary

Clouds and their feedbacks remain one of the largest uncertainties in predictions of future climate changes. High-resolution models can provide faithful simulations of clouds and their underlying turbulence in limited areas, but they have primarily been used in select locations, with limited success in reducing uncertainties in climate predictions. This study presents a framework for driving high-resolution simulations by a global climate model, which allows us to generate a library of high-resolution simulations across different cloud regimes. The framework leverages the potential of high-resolution models to improve parameterizations of clouds and turbulence in climate models and to better understand the cloud feedback mechanisms.

1 Introduction

General circulation model (GCM) predictions of the equilibrium climate sensitivity (ECS)—the equilibrium global mean surface temperature change after doubling of CO₂ concentrations—range between 2 K and 5 K across climate models (Knutti et al., 2017). This 3 K uncertainty has remained virtually unchanged for forty years (Charney et al., 1979), despite increases in the complexity of climate models and exponential increases in the computational power of high-performance computing (HPC) systems (Schneider, Teixeira, et al., 2017). Similar uncertainties exist in the transient climate response (Knutti et al., 2017). The largest uncertainties in model projections of climate change are traceable to the way in which these models represent boundary layer clouds and their climate feedbacks (Cess et al., 1990, 1996; Bony, 2005; Dufresne & Bony, 2008; Webb et al., 2006; Vial et al., 2013; Brient & Schneider, 2016; Brient et al., 2016). The challenge posed by clouds is that, on the one hand, their dynamics depend on small-scale processes, such as three-dimensional turbulence and microphysics, but on the other hand, they respond to and shape larger-scale atmospheric circulations. Thus, in coarse resolution GCMs, boundary-layer turbulence, convection, and clouds must be parameterized in terms of a GCM’s resolved fields. Inadequacies of these parameterizations are at the core of climate model uncertainties.

At the same time as the physical and computational complexity of GCMs has increased, expanding HPC capabilities have also enabled high-resolution, limited-area models, such as large-eddy simulations (LES), which directly resolve essential dynamics of turbulence, convection, and clouds. LES are being run with ever increasing resolution, on ever larger domains, and for ever longer durations. The ability of LES to provide high-fidelity simulations of boundary-layer turbulence, convection, and clouds is well estab-

66 lished (Siebesma et al., 2003; Matheou et al., 2011; Pressel et al., 2017; Schneider et al.,
 67 2019), making it a primary numerical laboratory for informing and validating climate
 68 model parameterizations. However, LES have so far mostly been used in selected loca-
 69 tions, usually associated with field campaigns, such as the often studied BOMEX (Siebesma
 70 et al., 2003), DYCOMS-II (Stevens et al., 2005), and RICO (Rauber et al., 2007) field
 71 campaigns. Some previous studies have used LES with idealized boundary conditions
 72 and large-scale forcings to investigate boundary layer dynamics in different dynamical
 73 regimes (e.g., Bellon & Stevens, 2012). Despite these attempts, the potential of LES to
 74 provide more systematic information for parameterizations across a broad cross-section
 75 of realistic dynamical regimes in a GCM has not been fully realized.

76 Here we describe an LES experimental design that allows us to explore a large range
 77 of atmospheric conditions encountered in a GCM. While driving limited-area models in
 78 idealized conditions in the tropics is well established (Sobel & Bretherton, 2000; Sobel
 79 et al., 2001), driving limited-area models with large-scale forcing from a GCM or a nu-
 80 merical weather prediction model in principle can be done anywhere in the atmosphere.
 81 However, it is less well established how to do so; see the discussion of potential pitfalls
 82 in Randall and Cripe (1999). A framework to drive LES with host models (GCMs or weather
 83 models) or reanalyses data is described by Neggers et al. (2012). In this framework, single-
 84 column models (SCMs) and/or LES are driven by prescribed large-scale forcing from host
 85 models or reanalyses, while being nudged toward the state of the host model or reanal-
 86 yses. The nudging prevents the LES from drifting away from the host model or reanal-
 87 ysis state. But it also constrains the turbulence developed by the LES, which limits the
 88 independent insights that can be gained from the LES in some dynamical regimes. This
 89 general approach has been used to study boundary layer dynamics and cloud feedbacks
 90 in selected locations and over long times (e.g., Schalkwijk et al., 2015; Dal Gesso & Neg-
 91 gers, 2018; Van Laar et al., 2019). Another approach to force LES with GCMs is one-
 92 way nesting (e.g., Dipankar et al., 2015; Heinze et al., 2017), where states at lateral bound-
 93 aries of the LES domain are relaxed toward those in a host model. The nesting approach
 94 allows for heterogeneous boundaries. But it requires LES on large domains, which is com-
 95 putationally expensive. In this study, we drive LES by dynamically consistent large-scale
 96 forcings given by a GCM and allow LES to evolve freely, without nudging in the atmo-
 97 sphere. We use the LES systematically to simulate clouds in different dynamical regimes.

98 To prove the concepts and for simplicity in illustrating them, the GCM here is the
 99 idealized moist GCM used in a number of studies of large-scale dynamics going back to
 100 Frierson et al. (2006) and O’Gorman and Schneider (2008). The GCM has simplified ra-
 101 diation and convection schemes, and there are no clouds in the model. We treat each LES
 102 as representing an idealized single grid column of the host GCM by prescribing terms
 103 in the water and thermodynamic budgets resolved by the GCM as forcing within the LES.
 104 The treatment of radiative transfer is identically simplified between the LES and GCM,
 105 allowing the LES to achieve a physically realizable atmospheric energy balance that is
 106 consistent with the GCM (albeit not necessarily realistic). Because the GCM’s resolved-
 107 scale fluxes that are applied to the LES do not directly include contributions from pa-
 108 rameterized turbulent and convective processes in the GCM, the LES responds by gen-
 109 erating a turbulent flow that closes the budgets. To the extent that the parameteriza-
 110 tions in the GCM are an accurate representation of the dynamics resolved by the LES,
 111 the LES and GCM should reach the same statistically steady states. The extent to which
 112 they do not do so reflects inadequacies in the parameterizations in the GCM, and the
 113 mismatches can be used to improve the parameterizations.

114 One unique aspect of this experimental design is that it allows an iterative work-
 115 flow to refine parameterizations that are implemented in a GCM. The iterative work-
 116 flow consists of the following steps:

- 117 1. Integrate the GCM to generate forcing data from selected GCM grid columns.

- 118 2. Integrate LES driven by forcing from the GCM columns.
- 119 3. Improve the GCM parameterizations by minimizing mismatches between the LES
- 120 and the GCM simulations for the selected columns.
- 121 4. Go to step 1.

122 GCM parameterizations can learn from offline LES simulations using data assim-
 123 ilation and machine learning approaches, and eventually, this workflow may be automated
 124 by spinning LES off the GCM simulation. Furthermore, experimental design approaches
 125 can be used to optimize the selection of GCM grid columns so as to be maximally in-
 126 formative about the parameterizations (Schneider, Lan, et al., 2017). We do not demon-
 127 strate this workflow in this paper; rather, this paper is a contribution within a larger re-
 128 search program with the goal to realize such an automated workflow.

129 The rest of the paper is organized as follows. Section 2 discusses the GCM and LES
 130 used to simulate the transition from shallow to deep convection across a Walker circu-
 131 lation. Section 3 describes how the GCM grid column budgets of temperature and wa-
 132 ter vapor are decomposed and then used to force the LES. Section 4 describes the sim-
 133 ulation characteristics in this forcing framework. Section 5 summarizes the conclusions
 134 and discusses the potential application of this framework to a range of cloud-climate prob-
 135 lems.

136 2 Model Descriptions

137 2.1 Moist Idealized General Circulation Model

138 The GCM simulations used in this work are performed using the moist idealized
 139 GCM described in Frierson et al. (2006) and O’Gorman and Schneider (2008). Moist con-
 140 vective processes are represented using a simplified quasi-equilibrium (Betts–Miller) scheme
 141 (Frierson et al., 2007), which assumes convection relaxes convectively unstable profiles
 142 towards moist-adiabatic reference profiles with a relative humidity of 70%. Precipita-
 143 tion is formed both by the parameterized convection and by large-scale condensation when
 144 a GCM grid box reaches saturation. Only liquid water (rain) is considered, and precip-
 145 itation is assumed to fall instantaneously to the surface. There are no clouds in the GCM.
 146 A k -profile eddy diffusivity scheme similar to that developed by Troen and Mahrt (1986),
 147 with a dynamically determined boundary layer height, is used to model turbulent trans-
 148 port within the atmospheric boundary layer. The atmosphere is assumed to overlay a
 149 40-m deep slab ocean, with which it interacts through radiative transfer and through la-
 150 tent and sensible heat fluxes. Surface fluxes of heat, moisture, and momentum are mod-
 151 eled using bulk aerodynamic formulas with drag coefficients determined from Monin-Obukhov
 152 similarity theory, with a roughness lengths of 1×10^{-5} m for all quantities. Atmospheric
 153 radiative transfer is represented by a two-stream semi-gray radiation scheme, where long-
 154 wave and shortwave absorption is calculated using prescribed latitudinally dependent ab-
 155 sorber profiles, as described in O’Gorman and Schneider (2008). The model does not have
 156 seasonal cycles or diurnal cycles.

157 The GCM simulations we perform are of a zonally asymmetric aquaplanet, in which
 158 zonal asymmetry is imparted by prescribing an ocean heat flux divergence (see Appendix
 159 A). The prescribed ocean heat flux divergence produces an off-equatorial Walker circu-
 160 lation, with suppressed convection in the region of maximum ocean heat flux divergence
 161 and enhanced convection in the region of maximum ocean heat flux convergence. Hav-
 162 ing a Walker circulation allows the LES driven by the aquaplanet GCM to generate some-
 163 what more realistic tropical cloud regimes than would be possible in a zonally symmet-
 164 ric setting. The GCM is run at T42 horizontal spectral resolution with 72 vertical lev-
 165 els (30 levels in the lowest 1.5 km) for a total of 3000 days. We accumulate forcing data
 166 to drive the LES from the last 500 days of the simulation. The dipole pattern of the pre-
 167 scribed ocean heat flux divergence (Figure 1a) induces zonal variations in surface tem-

168 peratures (Figure 1b) in the GCM. The zonally varying surface temperatures in turn drive
 169 an atmospheric Walker circulation, with strong ascent over warm temperatures and large-
 170 scale subsidence over cold temperatures (Figure 2). To drive the LES, we extract forc-
 171 ing data from selected GCM grid-columns along a transect connecting the points of max-
 172 imum and minimum ocean heat flux divergence (dots in Figure 1a).

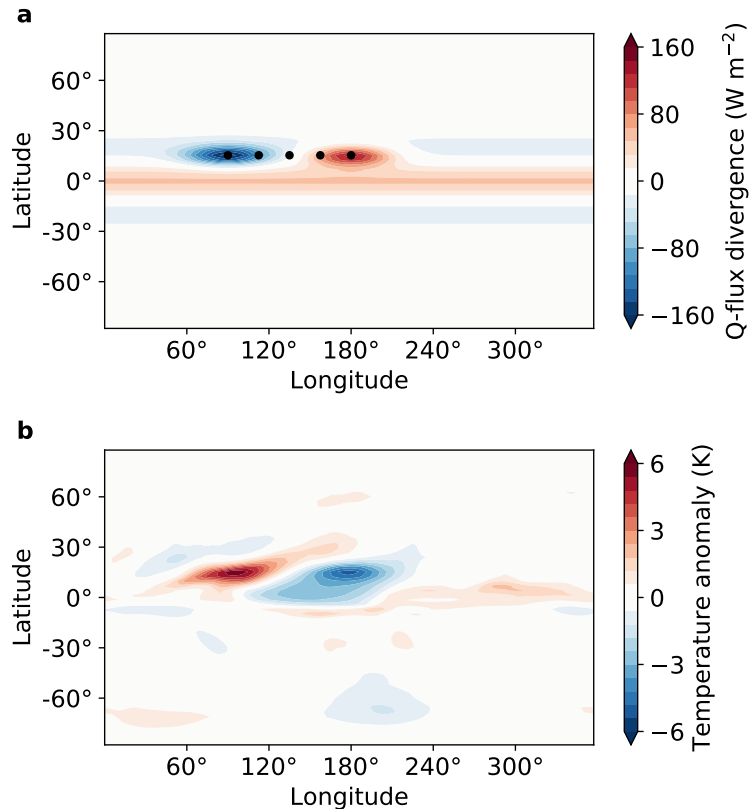


Figure 1. Surface fields in the GCM simulation. (a) Ocean heat flux divergence. (b) Surface temperature anomaly about zonal mean. Black circles indicate GCM grid columns along a transect connecting the regions of maximum and minimum ocean heat flux divergence.

173 2.2 Large-Eddy Simulation

174 The forcing framework is implemented in the Python Cloud Large-Eddy Simula-
 175 tion (PyCLES) code (Pressel et al., 2015). PyCLES is a parallel, three-dimensional LES
 176 code that solves the moist anelastic equations of motion (Pauluis, 2008), with prognos-
 177 tic equations for moist specific entropy s , total non-precipitating water specific humid-
 178 ity q_t , precipitating liquid water q_r (rain), and precipitating frozen water q_s (snow). The
 179 total water specific humidity includes contributions from water vapor q_v , non-precipitating
 180 liquid water q_l , and non-precipitating ice q_i , which are assumed to be in thermodynamic
 181 equilibrium. Along with dry air, these four components make up the thermodynamic sys-
 182 tem. The precipitating species are not assumed to be in thermodynamic equilibrium with
 183 q_t .

184 In PyCLES, the equations of motion are solved on a staggered, Arakawa-C grid (Arakawa
 185 & Lamb, 1977). The advection of both scalar and momentum fields are discretized us-

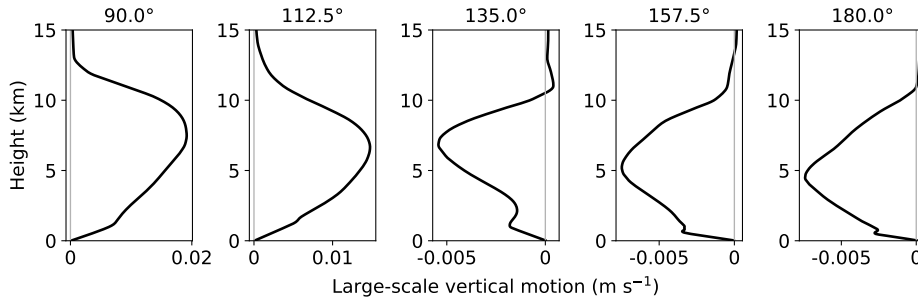


Figure 2. Vertical profiles of large-scale vertical motion in the GCM along the Walker circulation transect. The longitudes of the simulations are indicated above each panel.

186 ing nominally fifth-order weighted essentially non-oscillatory (WENO) schemes imple-
 187 mented as described in Pressel et al. (2015) and based on the schemes developed by Balsara
 188 and Shu (2000). Because of grid staggering, the actual accuracy of the WENO schemes
 189 is limited to second order. The pressure is diagnosed following Pressel et al. (2015), and
 190 time-stepping is performed using a second-order strong stability preserving Runge-Kutta
 191 scheme (Shu & Osher, 1988). The numerical formulation does not ensure monotonicity
 192 or positivity of solutions, so clipping is employed when needed to ensure that fields such
 193 as specific humidities that need to remain positive do indeed remain positive. Subgrid-
 194 scale (SGS) fluxes of momentum and scalars are modeled through the Smagorinsky-Lilly
 195 closure (Lilly, 1962; Smagorinsky, 1963), with the Smagorinsky coefficient $c_s = 0.17$ and
 196 the turbulent Prandtl number $Pr_t = 1/3$.

197 The formation and fate of precipitating species is represented using a single-moment,
 198 bulk microphysical model based on the scheme developed by Kaul et al. (2015); differ-
 199 ences between their scheme and that used here are enumerated in Appendix B. Precip-
 200 itation that reaches the surface is assumed to fall out of the atmosphere, with no trans-
 201 fer of energy or mass to the ocean. The LES are forced with prescribed sea surface tem-
 202 peratures from the GCM. It is tempting to allow the surface temperatures in LES to vary
 203 by coupling the simulations with a slab ocean; however, we found that doing so leads to
 204 significant drift of the LES away from the GCM state in deep convection regions, pre-
 205 sumably because of inadequacies of the simple turbulence and convection parameteri-
 206 zations employed in the GCM. Surface fluxes are modeled using bulk aerodynamic for-
 207 mulas based on Monin-Obukhov similarity theory. Radiative transfer is represented iden-
 208 tically to the scheme used in GCM, with no effects of clouds on the radiative transfer.

209 We run LES driven by the GCM fields into a statistically steady state. This is com-
 210 putationally expensive for several reasons. First, we simulate a large, three-dimensional,
 211 doubly periodic domain that is 64 km wide and 25.6 km high, to be able to simulate deep
 212 convection. Second, the timescale for the LES to reach a statistically steady state is set
 213 by the timescale over which the atmosphere equilibrates, which can take tens of days.
 214 To reduce the computational cost we run the LES at a relatively coarse resolution of 250 m.
 215 The vertical grid is stretched and consists of 256 grid points. The vertical resolution de-
 216 creases from about 50 m near the surface to around 200 m at the domain top. The sim-
 217 ulations are run for 60 days (90.0° and 112.5°), 90 days (135.0°), or 180 days (157.5° and
 218 180.0°). The results in this study are averaged over the last 15 simulated days, when the
 219 simulations have reached statistically steady states.

3 Forcing Framework

3.1 GCM Equations

Our goal is to develop an LES forcing framework in which the LES emulates a single grid column of a GCM, directly resolving processes that are parameterized in the GCM while satisfying the same large-scale water and thermodynamic balances as the GCM. To achieve this, we begin by considering the equations for the grid-scale temperature \tilde{T} and specific humidity \tilde{q}_t that are resolved by the GCM. Tildes ($\tilde{\cdot}$) denote variables resolved on the GCM grid. The thermodynamic equation in the GCM's σ coordinates is given by (Durran, 1999)

$$\underbrace{\partial_t \tilde{T} + \tilde{u} \partial_x \tilde{T} + \tilde{v} \partial_y \tilde{T} + \tilde{\omega} \partial_\sigma \tilde{T} - \frac{\tilde{\alpha} \tilde{\omega}}{c_p}}_{\text{GCM-Resolved Dynamics}} = \underbrace{\tilde{J}_{\text{conv}} + \tilde{J}_{\text{cond}} + \tilde{J}_{\text{diff}} + \tilde{J}_{\text{numerical}} + \tilde{J}_{\text{rad}}}_{\text{GCM Parameterized}}, \quad (1)$$

which we have written such that the left hand side of the equation is the sum of the time-tendency of temperature and GCM-resolved advection terms, while the right hand side consists of parameterized source terms arising from the deep convection scheme (\tilde{J}_{conv}), large-scale condensation (\tilde{J}_{cond}), diffusive parameterizations such as the boundary layer turbulence scheme (\tilde{J}_{diff}), the radiation scheme (\tilde{J}_{rad}), and numerical damping and spectral filtering ($\tilde{J}_{\text{numerical}}$). Here, $\sigma = \tilde{p}/\tilde{p}_s$, with pressure \tilde{p} and surface pressure \tilde{p}_s , $\tilde{\omega} = d\sigma/dt$, $\tilde{\omega} = d\tilde{p}/dt$, $\tilde{\alpha}$ is the specific volume, and c_p is the specific heat capacity of dry air; the notation is otherwise standard. (We use Cartesian coordinates to simplify the notation; however, the GCM uses spherical coordinates, whereas the LES is Cartesian.) Similarly, the GCM's specific humidity budget is given by

$$\underbrace{\partial_t \tilde{q}_t + \tilde{u} \partial_x \tilde{q}_t + \tilde{v} \partial_y \tilde{q}_t + \tilde{\omega} \partial_\sigma \tilde{q}_t}_{\text{GCM-Resolved Dynamics}} = \underbrace{\tilde{S}_{\text{conv}} + \tilde{S}_{\text{cond}} + \tilde{S}_{\text{diff}}}_{\text{GCM Parameterized}}. \quad (2)$$

In a statistically steady state, the explicit time derivatives vanish upon long-term time averaging, and the parameterized processes on the right-hand sides balances with resolved-scale flows of \tilde{T} and \tilde{q}_t on the left-hand sides. Our goal is to impose the resolved-scale budget terms on the left-hand side of equations (1) and (2) on the LES, while allowing the LES to generate a three-dimensional turbulent flow, microphysical processes, and radiative energy fluxes that determine the terms on the right-hand sides of the same equations. Here we implement long-time mean forcing from statistically steady states of the GCM, without the explicitly time dependent terms; however, it is straightforward to drive the LES using time-varying forcing from the GCM consistent with equations (1) and (2). We limit the present study to simulations using long-time mean forcing because time varying forcing includes synoptic scale variability which would require much longer LES simulations to achieve statistically robust results.

3.2 Specific Humidity Forcing

In the LES, we modify the prognostic equation for total water specific humidity to include additional source terms S_{hadv} and S_{vadv} arising from GCM-resolved horizontal and vertical advection, giving

$$\partial_t q_t + \partial_x (u q_t) + \partial_y (v q_t) + \rho_0^{-1} \partial_z (\rho_0 \omega q_t) = -\partial_x (\gamma_{q,x}) - \partial_y (\gamma_{q,y}) - \rho_0^{-1} \partial_z (\rho_0 \gamma_{q,i}) + E - P + S_{\text{hadv}} + S_{\text{vadv}}, \quad (3)$$

where ρ_0 is the reference density, $\gamma_{q,x}$, $\gamma_{q,y}$, and $\gamma_{q,z}$ are the SGS fluxes of q_t , and E and P are source terms due to evaporation and production of hydrometeors. Consistent with Randall and Cripe (1999), we prescribe the horizontal advective source term directly from the GCM such that

$$S_{\text{hadv}} = -\langle \tilde{u} \partial_x \tilde{q}_t \rangle - \langle \tilde{v} \partial_y \tilde{q}_t \rangle, \quad (4)$$

266 where $\langle \cdot \rangle$ indicates a long-time mean on σ surfaces in the statistically steady state of the
 267 GCM.

268 Specification of the vertical advection source term is more complicated because the
 269 LES produces its own vertical advection, acting on its own domain-mean vertical gra-
 270 dients. We compute the vertical advection source term by rewriting the vertical advec-
 271 tion term in equation (2) using the hydrostatic relation and decomposing it into time
 272 mean and fluctuating components as

$$273 \quad \langle \tilde{\omega} \partial_\sigma \tilde{q}_t \rangle \approx \langle \tilde{w} \rangle \partial_z \langle \tilde{q}_t \rangle + \langle \tilde{w}' \partial_z \tilde{q}_t' \rangle, \quad (5)$$

274 where $w = dz/dt$ is the vertical velocity and primes $(\cdot)' = (\cdot) - \langle \cdot \rangle$ denote fluctuations
 275 about the time mean $\langle \cdot \rangle$. We approximate the time-averaged vertical velocity by $\langle \tilde{w} \rangle \approx$
 276 $-\langle \tilde{\omega} \rangle \langle \tilde{\alpha} \rangle / g$ where we have assumed that $\tilde{\omega}$ and $\tilde{\alpha}$ are uncorrelated. Replacing the GCM
 277 specific humidity \tilde{q}_t with the LES specific humidity q_t then gives the vertical advection
 278 source term we apply to the LES:

$$279 \quad S_{\text{vadv}} = -\langle \tilde{w} \rangle \partial_z q_t - \langle \tilde{w}' \partial_z \tilde{q}_t' \rangle. \quad (6)$$

280 The first term on the right-hand side accounts for vertical advection of q_t by GCM-resolved
 281 time-mean vertical motion. The second term accounts for vertical fluxes associated with
 282 fluctuations about the long-time mean and is prescribed directly from the GCM; it is typ-
 283 ically much smaller than the mean component.

284 3.3 Specific Entropy Forcing

285 We modify the LES prognostic equation for moist specific entropy to include source
 286 terms owing to GCM-resolved transports of total water specific humidity and temper-
 287 ature, such that

$$288 \quad \partial_t s + \partial_x (us) + \partial_y (vs) + \rho_0^{-1} \partial_z (\rho_0 ws) = -\partial_x (\gamma_{s,x}) - \partial_y (\gamma_{s,y}) - \rho_0^{-1} \partial_z (\rho_0 \gamma_{s,z}) \\ 289 \quad + \frac{c_p}{T} J_{\text{rad}} + \dot{S} + \frac{c_p}{T} (J_{\text{hadv}} + J_{\text{vadv}}) + (s_v - s_d) (S_{\text{hadv}} + S_{\text{vadv}}), \quad (7)$$

290 where $\gamma_{s,x}$, $\gamma_{s,y}$, and $\gamma_{s,z}$ are the SGS fluxes of s and J_{rad} is the source term due to ra-
 291 diation. The term \dot{S} represents irreversible entropy sources associated with the SGS dy-
 292 namics and precipitation processes, as described in Pressel et al. (2017). The last two
 293 terms on the right-hand side arise from the GCM-resolved advective tendencies of tem-
 294 perature (J_{hadv} and J_{vadv}) and total water specific humidity (S_{hadv} and S_{vadv}), and s_v
 295 and s_d are specific entropies of dry air and water vapor, respectively. Consistent with
 296 Randall and Cripe (1999) and the treatment of total water specific humidity in section 3.2,
 297 we take the horizontal advective temperature tendency J_{hadv} directly from the GCM,
 298 such that

$$299 \quad J_{\text{hadv}} = -\langle \tilde{u} \partial_x \tilde{T} \rangle - \langle \tilde{v} \partial_y \tilde{T} \rangle + \langle \tilde{J}_{\text{numerical}} \rangle. \quad (8)$$

300 The vertical advective temperature tendency J_{vadv} , including the pressure-volume work
 301 term $\tilde{\alpha} \tilde{\omega} / c_p$, is derived by using the hydrostatic approximation to approximate the last
 302 term on the left-hand side of (1),

$$303 \quad \left\langle \tilde{\omega} \partial_\sigma \tilde{T} - \frac{\tilde{\alpha} \tilde{\omega}}{c_p} \right\rangle \approx \langle \tilde{w} \rangle \partial_z \langle \tilde{T} \rangle + \langle \tilde{w}' \partial_z \tilde{T}' \rangle + \langle \tilde{w} \rangle \frac{g}{c_p}. \quad (9)$$

304 Here, we have used again the approximation $\langle \tilde{w} \rangle \approx -\langle \tilde{\omega} \rangle \langle \tilde{\alpha} \rangle / g$. Replacing the GCM
 305 temperature \tilde{T} with the LES temperature T in the first term on the right-hand side then
 306 gives the vertical transport applied to the LES as

$$307 \quad J_{\text{vadv}} = -\langle \tilde{w} \rangle \partial_z T - \langle \tilde{w}' \partial_z \tilde{T}' \rangle - \langle \tilde{w} \rangle \frac{g}{c_p}, \quad (10)$$

308 with the second and third terms on the right-hand side taken directly from the GCM.

311 While we have discussed the forcing framework for an LES using specific entropy
 312 as a prognostic variable, it is straightforward, and in some ways easier, to implement it
 313 in models using other formulations of moist thermodynamics. For example, in an LES
 314 using some variety of liquid-ice potential temperature as a prognostic variable, the for-
 315 mulation of the specific humidity forcing is identical to that described here, and the GCM-
 316 resolved transport terms in the potential temperature equations are analogous to the terms
 317 involving $J_{\text{hadv/vadv}}$ on the right-hand side of equation (7) but with the inverse Exner
 318 function replacing $1/T$.

319 3.4 Momentum Forcing

320 The LES horizontal momentum field is driven by the large-scale pressure gradient
 321 from the GCM and Coriolis acceleration. The LES horizontal momentum equations are
 322 modified to be

$$323 \partial_t u + \partial_x (uu) + \partial_y (uv) + \rho_0^{-1} \partial_z (\rho_0 uw) = -\partial_x (\rho_0^{-1} p') \\ 324 - \partial_x \tau_{xx} - \partial_y \tau_{xy} - \rho_0^{-1} \partial_z (\rho_0 \tau_{xz}) - f (\langle \tilde{v}_g \rangle - v), \quad (11)$$

327 and

$$328 \partial_t v + \partial_x (uv) + \partial_y (vv) + \rho_0^{-1} \partial_z (\rho_0 vw) = -\partial_y (\rho_0^{-1} p') \\ 329 - \partial_x \tau_{yx} - \partial_y \tau_{yy} - \rho_0^{-1} \partial_z (\rho_0 \tau_{yz}) + f (\langle \tilde{u}_g \rangle - u) \quad (12)$$

332 where τ represents the SGS stress, and $\langle \tilde{u}_g \rangle$ and $\langle \tilde{v}_g \rangle$ are the mean zonal and meridional
 333 geostrophic winds from the GCM.

334 It is tempting to impose the GCM-resolved horizontal momentum budgets on the
 335 LES in an analogous approach to the imposition of the GCM-resolved thermodynamic
 336 and water budgets, rather than just imposing the GCM large-scale pressure gradient.
 337 However, we found that doing so leads to strong inertial oscillations in the LES.

338 3.5 Radiation

339 One essential aspect of this framework is that the representation of radiative trans-
 340 fer implemented in the LES should be identical to that implemented in the GCM. This
 341 enables controlled numerical experiments that isolate differences between resolved tur-
 342 bulence, convection, and clouds in the LES from their parameterized counterparts in the
 343 GCM. Furthermore, using the same representation of radiative transfer guarantees that,
 344 at least initially, free-troposphere large-scale transport imposed on the LES from the GCM
 345 is balanced by radiative heating/cooling, thus preventing the free-troposphere temper-
 346 ature from drifting. This is why we employ the same two-stream gray radiation scheme,
 347 without cloud radiative effects, in both the LES and the GCM.

348 3.6 Surface fluxes

349 Surface fluxes are modeled using a bulk scheme with drag coefficients obtained from
 350 Monin-Obukhov similarity theory (Byun, 1990). Since we are using the time-mean forc-
 351 ing from the GCM, the variation in surface wind speed in the LES is much smaller than
 352 in the GCM. This leads to significant differences in surface fluxes between the GCM and
 353 LES, which affects the temperature profile. To account for synoptic variability, we mod-
 354 ify the surface wind speed to add a gustiness when calculating surface fluxes in the LES.
 355 The gustiness is estimated by the standard deviation of 6-hourly wind speed at the low-
 356 est model level in the GCM, which decreases from 3.20 m s^{-1} over the warmest surface
 357 temperature to 1.49 m s^{-1} over the coldest surface temperature.

358

3.7 Interpolation

359

360

361

362

363

364

365

366

367

368

369

370

371

372

The GCM and LES use different vertical grids (σ vs. z coordinates). Therefore, vertical profiles extracted from the GCM must be interpolated onto the LES vertical grid. We do so by interpolating from the GCM's σ levels onto the LES's height levels using the time-mean height of each σ level at the horizontal location in question. This represents an additional approximation because averages at constant σ and constant z differ. One of two interpolation methods is used depending on whether the gradient of the interpolated field appears explicitly in the forcing. For variables that do not appear inside a gradient (e.g., u , v , or J_{hadv}), the GCM profiles are interpolated using a monotonic piecewise cubic Hermite interpolating polynomial (PCHIP). For interpolated variables that do appear inside a gradient (e.g., q_t or T), the vertical derivative of the field on the GCM grid is interpolated to the LES vertical grid using a PCHIP interpolation, and the value of the field is recovered by numerically integrating the interpolated derivative using the trapezoidal rule. This approach ensures a nearly monotonic interpolation of discrete derivatives of the field.

373

3.8 LES Initial Condition

374

375

376

377

378

379

The LES initial conditions are specified from the GCM statistically steady-state mean vertical profiles of temperature, specific humidity, and horizontal wind speed. Starting with this initial condition helps because it ensures that where parameterized processes in the GCM vanish, the GCM-resolved forcing terms balance (up to small differences arising mostly from numerical interpolation error), provided the treatment of radiative transfer is identical in both models.

380

4 Simulation Characteristics

381

382

383

384

385

386

387

388

Figure 3 shows the timeseries of outgoing longwave radiation in the LES and illustrates the time it takes to equilibrate to a statistically steady state. The simulations reach steady state more rapidly in deep convection regions than in shallow convection regions, and all cases are in statistically steady state by the end of the simulations. As the LES are free to evolve from their initial condition, which is specified to be the long-time mean of the GCM, their equilibrated solution can diverge substantially from their initial state. The differences between the equilibrated LES solution and GCM long-time means can be used to identify deficiencies in GCM parameterizations.

389

390

391

392

393

394

395

396

397

398

399

400

401

402

403

404

405

406

407

Figure 4 shows the equilibrium temperature and relative humidity profiles in the GCM and in the LES along the Walker circulation transect. The temperature profiles are in general very similar between the GCM and LES, except that in the free troposphere the LES is slightly cooler than the GCM at 135.0° longitude, which is consistent with the lower OLR in the LES (Figure 3). There are larger differences in the relative humidity profiles. The GCM-simulated relative humidity in deep convection regions is close to 70% in the free troposphere. The relative humidity has a local maximum of about 90% near 1 km and decreases to about 60% near the surface. The relative humidity in the LES is higher than that in the GCM both in the free troposphere and near the surface. The difference in relative humidity between GCM and LES arises because in deep convection regions, convection is occurring most of the time, and the difference shows the deficiency of the simple GCM convection scheme. In the LES, convection keeps the relative humidity at a high value, while in the GCM, the simple convection scheme keeps the relative humidity close to the reference value (0.7). The jump in relative humidity at about 5 km in the LES results from the cooling effect of snow melting. In shallow convection regions, the relative humidity in the GCM has local maxima near the surface and the tropopause and a local minimum in the middle of the troposphere. The LES produces a much moister free troposphere at 135.0° longitude, which may be related to the lower tropospheric temperature in the LES. The simulations with lower surface temper-

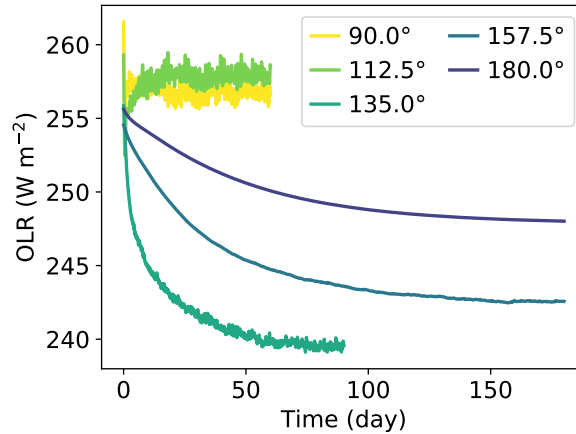


Figure 3. Timeseries of LES outgoing longwave radiation (OLR) at various longitudes along the Walker circulation transect.

408 atures (157.5° and 180.0°) in general resemble the GCM, with a slightly larger relative
 409 humidity in the LES.

410 Figure 5 shows the equilibrium surface fluxes and surface precipitation in the GCM
 411 and LES. The latent heat flux decreases from about 300 W m^{-2} in deep convection re-
 412 gions to less than 100 W m^{-2} in shallow convection regions in the GCM. The sensible
 413 heat flux and net longwave radiative flux show similar differences between deep and shal-
 414 low convection regions, although the magnitudes are smaller. In the LES, the latent heat
 415 flux is weaker by 20-25% in deep convection regions, consistent with the higher relative
 416 humidity in the boundary layer (Figure 4b). The decrease in the latent heat flux is par-
 417 tially balanced by increases in the net upward longwave radiative flux and in the sensi-
 418 ble heat flux, which result from an increase in the temperature difference between the
 419 surface and near-surface air. The surface fluxes in shallow convection regions are sim-
 420 ilar between the GCM and LES. The LES generally reproduces the spatial pattern of
 421 surface precipitation in the GCM, with strong precipitation in deep convection regions
 422 and weak or no precipitation in shallow convection regions along the transect. In deep
 423 convection regions, the surface precipitation is weaker in the LES than that in the GCM.

424 To further understand the difference between the GCM and LES, we compare ver-
 425 tically integrated moisture and dry enthalpy budgets (Figure 6). Note that the tenden-
 426 cies from horizontal advection in the LES are directly prescribed and are the same as
 427 those in the GCM. Since we focus on a statistically steady state, the sum of different terms
 428 affecting the budget is approximately zero. In deep convection regions, the moisture bud-
 429 get is kept in balance mainly by vertical advection, precipitation, and evaporation. The
 430 decreased evaporation in the LES is balanced by the decreased precipitation and the strength-
 431 ened vertical advection of water vapor out of the moister boundary layer (Figure 4b).
 432 The dry enthalpy budget is kept in balance mainly by vertical advection, latent heat of
 433 precipitation, and radiation. The decrease in latent heat from precipitation in the LES
 434 is mainly balanced by the weaker radiative cooling and weaker adiabatic cooling from
 435 vertical motion. In the shallow convection regions, the main terms controlling the mois-
 436 ture budget are subsidence drying and evaporation, and the main terms controlling the
 437 dry enthalpy budget are subsidence warming and radiative cooling. The budgets are con-
 438 sistent between the GCM and LES in shallow convection regions.

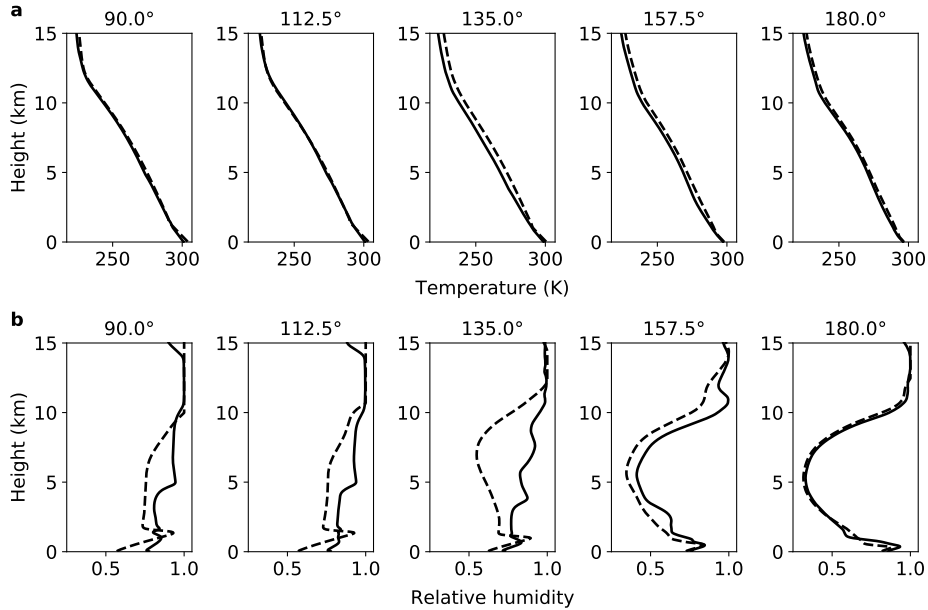


Figure 4. Vertical profiles of (a) temperature and (b) relative humidity along the Walker circulation transect in the GCM (dashed) and in the LES (solid). The relative humidity is the weighted average with respect to liquid and ice. The longitudes of the simulations are indicated above each panel.

439 Figure 7 shows the vertical profiles of different terms balancing moisture and temperature budgets at two longitudes in deep and in shallow convection regions. At 90.0°,
 440 the moisture budget is mainly balanced by vertical advection and turbulent and convective drying, and the temperature budget is mainly balanced by vertical advection, turbulent and convective heating, and radiative cooling. The vertical structure of the tendencies is broadly consistent between the GCM and LES, with some differences in the boundary layer and near the melting level. The mismatch between the GCM and LES
 441 near the boundary layer top is related to the local minimum in moisture in the LES (Figure 4b). At 180.0°, the moisture budget is mainly balanced by subsidence drying and turbulent and convective moistening in the cloud layer, and by subsidence drying and horizontal advection in the free troposphere. The GCM-LES difference in the moisture
 442 budget below 1 km suggests that the GCM has a shallower boundary layer and weaker convection than the LES. The temperature budget is mainly balanced by subsidence warming and radiative cooling. The GCM and LES agree well on the temperature budget at
 443 180.0°, as expected from the similar temperature profiles (Figure 4a).

454 Figure 8 shows the vertical profiles of cloud fraction and cloud water specific humidity along the Walker cell transect in the LES. The simulation with the coldest surface temperature (180.0°) produces a very shallow and thin cloud layer with cloud base around 300 m and cloud top around 1000 m. Below the cloud base, there is a well-mixed boundary layer, as seen in the vertical profiles of liquid-ice potential temperature and total water specific humidity (Figure 9). The well-mixed boundary layer and the shallow-cumulus layer deepen as the surface temperature increases. The simulation at 135.0° longitude develops a secondary maximum in cloud fraction at about 4 km, which originates from the cooling effects of snow melting. The cloud water specific humidity (the sum of the cloud liquid and ice specific humidities) has a similar vertical structure as the cloud
 455
 456
 457
 458
 459
 460
 461
 462
 463

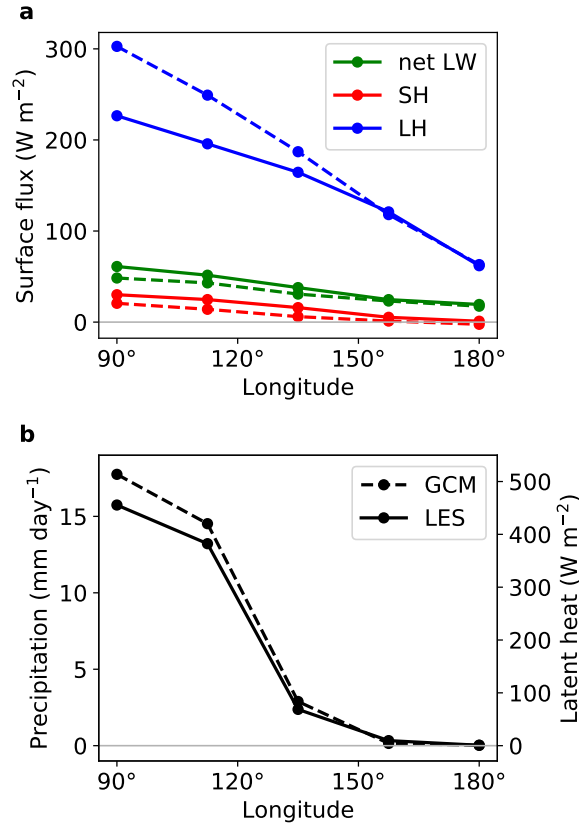


Figure 5. (a) Equilibrium surface fluxes in the GCM (dashed) and LES (solid). Green lines denote net longwave radiative flux, red lines sensible heat flux, blue lines latent heat flux. (b) Surface precipitation along the Walker circulation transect in the GCM (dashed) and LES (solid). The latent heat associated with precipitation is shown on the right vertical axis.

464 fraction in shallow convection regions. As the surface temperature increases along the
 465 transect, the LES produce a transition to deep convection at 90.0° and 112.5° longitudes.
 466 The simulations produce anvil clouds with a peak in cloud fraction at about 11 km. There
 467 is a secondary maximum in cloud fraction near the melting level at about 5 km, which
 468 has also been reported in previous observational and high-resolution modeling studies
 469 (Posselt et al., 2008; Stein et al., 2011). The vertical profile of cloud water specific hu-
 470 midity is more bottom-heavy than that of cloud fraction, with a more obvious peak near
 471 the melting level. In general, the LES produce little cloud ice in the upper troposphere
 472 in deep convection regions, which may be related to the relatively simple microphysics
 473 scheme and the lack of cloud-radiation interactions (Hartmann et al., 2018) in this study.

474 5 Discussion and Conclusions

475 We have described a framework in which LES are driven by large-scale forcing taken
 476 from an idealized aquaplanet GCM, in a one-way coupling setup. The LES are forced
 477 with prescribed SST from the GCM, but they are otherwise freely evolving, without the
 478 direct constraints on temperature or humidity profiles that are usually imposed in LES
 479 studies. Instead, we imposed GCM-resolved, large-scale energy and moisture budget terms
 480 as forcing terms in the LES. We also imposed the large-scale pressure gradient from the

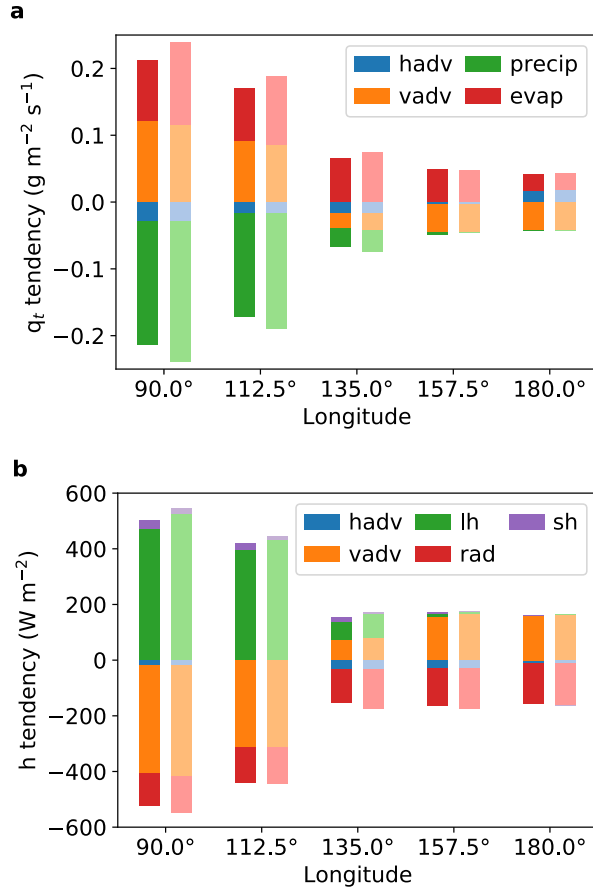


Figure 6. (a) Vertically integrated moisture tendencies from horizontal advection (hadv), vertical advection (vadv), precipitation (precip), and evaporation (evap). (b) Vertically integrated dry enthalpy tendencies from horizontal advection, vertical advection, latent heat of precipitation (lh), surface sensible heat flux (sh), and radiation (rad). Upward bars show sources and downward bars show sinks. LES and GCM budgets are shown in darker and lighter colors, respectively.

481 GCM to drive the LES horizontal wind. Both the LES and GCM include the same ra-
 482 diative transfer schemes. This allows us to generate LES in grid columns of GCMs and
 483 to provide suitable benchmarks for testing and calibration of parameterization schemes
 484 in GCMs.

485 To illustrate the concepts, we used this forcing framework to simulate the transi-
 486 tion from shallow to deep convection along an idealized Walker circulation transect. The
 487 Walker circulation is induced by prescribing a dipole structure of ocean heat flux con-
 488 vergence/divergence in the slab ocean of the GCM. LES driven by large-scale forcing from
 489 the GCM reach statistically steady states without nudging toward reference profiles. The
 490 LES are able to reproduce the longitudinal variation of relative humidity, surface fluxes,
 491 and precipitation, with some mismatches to the GCM climatology, especially in deep con-
 492 vection regions. The mismatches are indicative of inadequacies in the GCM's convection
 493 parameterization, which is unsurprising given the simplicity of the parameterization. The

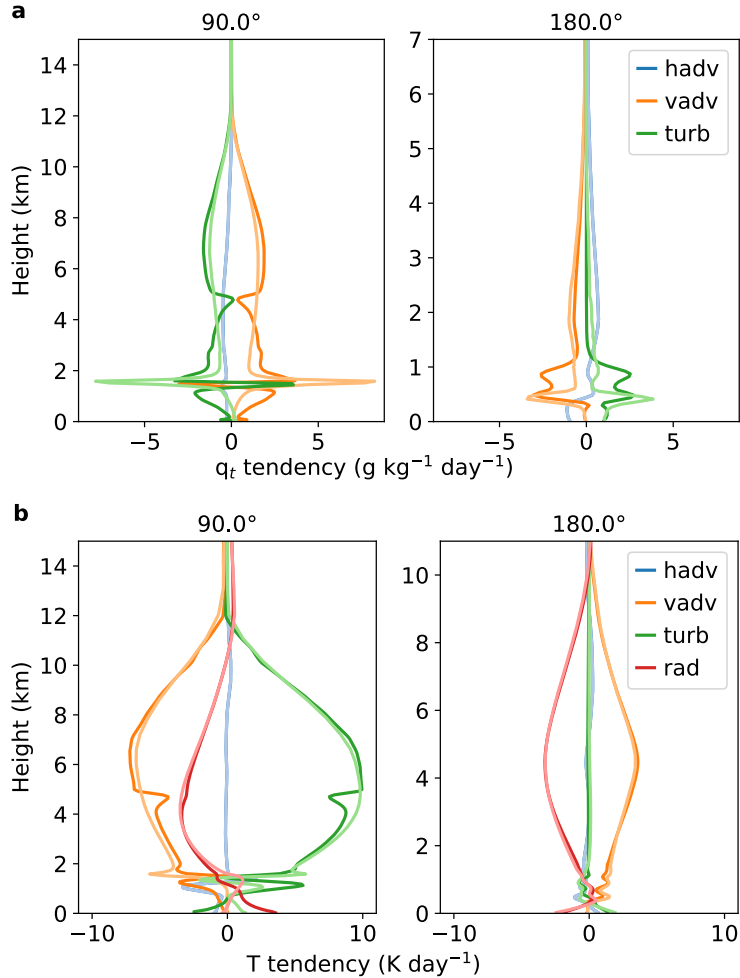


Figure 7. (a) Vertical profiles of moisture tendencies from horizontal advection (hadv), vertical advection (vadv), and turbulence and convection (turb). (b) Vertical profiles of temperature tendencies from horizontal advection, vertical advection, turbulence and convection, and radiation (rad). LES and GCM budgets are shown in darker and lighter colors, respectively. The longitudes of the simulations are indicated above each panel.

494 mismatches can be used to systematically improve parameterization schemes, for exam-
 495 ple, with Bayesian calibration methods (Schneider, Lan, et al., 2017).

496 Our idealized setup has limitations. The gray radiation scheme we used to prove
 497 the concept does not depend on water vapor concentration or cloud properties. This dis-
 498 torts the radiative driving of the flows relative to what would happen in reality. The cou-
 499 pling of clouds, water vapor, and radiation has been shown to affect the Intertropical Con-
 500 vergence Zone and anvil clouds in deep convection regions (Voigt & Shaw, 2015; Dixit
 501 et al., 2018; Hartmann et al., 2018), as well as boundary layer clouds, the diurnal cycle
 502 of shallow cumulus, and the stratocumulus-to-cumulus transition (Xiao et al., 2014; Vial
 503 et al., 2019). The resolution of LES used in this study (250 m) is not fine enough to fully
 504 resolve low clouds. Deep convective clouds are sensitive to microphysical processes, which
 505 are parameterized in a simple way in our model. These factors may contribute to the
 506 relatively small cloud fraction and cloud water path in our simulations of shallow cumu-

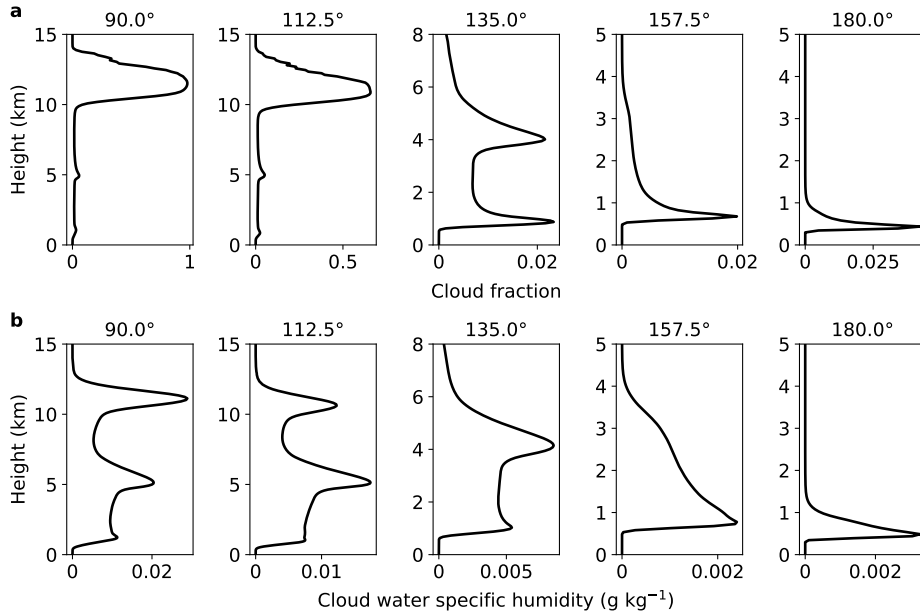


Figure 8. Vertical profiles of (a) cloud fraction and (b) cloud water specific humidity along the Walker circulation transect in the LES. The longitudes of the simulations are indicated above each panel.

507 lus, and to the relatively small amount of cloud ice in deep convection regions. These
 508 shortcomings limit the applicability of the results to some extent. But the simplifications
 509 facilitated the development and testing of the framework and suffice in a proof-of-concept
 510 that illustrates its usability. They also simplify interpretation, for example, of the cloud
 511 response to climate change.

512 We are currently using this framework to study cloud–climate feedbacks in an ide-
 513 alized setting and to generate a library of LES simulations for developing and training
 514 more comprehensive GCM parameterizations than the ones we used here. A library con-
 515 taining a wide range of LES across different cloud regimes, including LES of changed cli-
 516 mates, provides a powerful opportunity to systematically train complex dynamical pa-
 517 rameterizations, with minimal imprinting of the GCM’s parameterizations onto the LES
 518 forcing (the only imprinting occurs through the dependence of the large-scale advection
 519 terms on the dynamical parameterizations). It thereby enables direct and meaningful
 520 tests of the parameterizations against LES. An LES library including simulations of changed
 521 climates not only enables tests of parameterizations but also provides an opportunity
 522 to investigate cloud feedbacks in LES that are not subject to nudging to reference pro-
 523 files or ad hoc assumptions about how large-scale dynamics change with climate. The
 524 results of climate change simulations will be described in a companion paper.

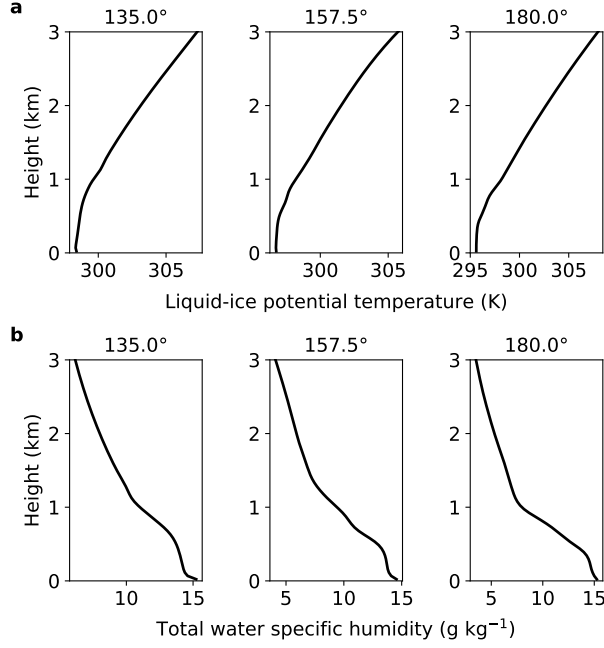


Figure 9. Vertical profiles of (a) liquid-ice potential temperature and (b) total water specific humidity in shallow convection regions. The longitudes of the simulations are indicated above each panel.

Appendix A Ocean Heat Flux

The time-independent ocean heat flux divergence (O) prescribed in the GCM is of the following form:

$$O = Q_0 \left(1 - \frac{2\phi^2}{\phi_0^2} \right) \exp \left(-\frac{\phi^2}{\phi_0^2} \right) - Q_1 \exp \left(-\frac{D(\eta, \eta_e)^2}{\eta_1^2} - \frac{(\phi - \phi_n)^2}{\phi_1^2} \right) + Q_1 \exp \left(-\frac{D(\eta, \eta_w)^2}{\eta_1^2} - \frac{(\phi - \phi_n)^2}{\phi_1^2} \right). \quad (\text{A1})$$

Here, ϕ is latitude and η is longitude. The first term on the right-hand side represents the hemispherically and zonally symmetric component of ocean heat flux divergence away from the equator, as in Bordoni and Schneider (2008) and Merlis and Schneider (2011). The second and third terms represent the zonally asymmetric components, similar to Merlis and Schneider (2011). The asymmetric component of the heat fluxes takes the form of a dipole in the northern hemisphere centered at $\phi_n = 15.0^\circ$ latitude, with cooling and warming lobes centered at $\eta_w = 90.0^\circ$ and $\eta_e = 180.0^\circ$ longitude. D is the distance between two longitudes η_a and η_b , defined as $D(\eta_a, \eta_b) = \min(|\eta_a - \eta_b|, 360^\circ - |\eta_a - \eta_b|)$. The parameters we chose are $\phi_0 = 16.0^\circ$, $\eta_1 = 30.0^\circ$, $\phi_1 = 6.0^\circ$, $Q_0 = 50 \text{ W m}^{-2}$, and $Q_1 = 150 \text{ W m}^{-2}$.

Appendix B Microphysics

Our microphysics scheme is similar to Arctic mixed-phase scheme described in Kaul et al. (2015) in that it is a one-moment microphysical parameterization with prognostic equations for precipitating water and ice. Our microphysics differs from that in Kaul et al. (2015) primarily in the liquid fraction function $\lambda(T)$, which determines the phase

547 partitioning between cloud liquid and ice:

$$548 \quad \lambda(T) = \begin{cases} 0 & T < T_i, \\ \frac{T-T_i}{T_f-T_i} & T_i < T \leq T_f, \\ 1 & T > T_f. \end{cases} \quad (\text{B1})$$

549 Here, we use $T_i = 263.15$ K and $T_f = 273.15$ K. Further, our scheme replaces the cloud
550 ice and snow auto-conversion rate closures used in Kaul et al. (2015) with those used in
551 Grabowski (1998), which are more appropriate for use in simulations of subtropical and
552 tropical convection.

553 Acknowledgments

554 We gratefully acknowledge the generous support of Eric and Wendy Schmidt (by rec-
555 ommendation of Schmidt Futures), Mountain Philanthropies, Charles Trimble, the Paul
556 G. Allen Family Foundation, and the National Science Foundation (grant 1835860). The
557 simulations were performed on Caltech’s High Performance Cluster, which is partially
558 supported by a grant from the Gordon and Betty Moore Foundation. The GCM and Py-
559 CLES codes are available online at <http://climate-dynamics.org/software>.

560 References

- 561 Arakawa, A., & Lamb, V. R. (1977). Computational Design of the Basic Dynamical
562 Processes of the UCLA General Circulation Model. In J. Chang (Ed.), *Methods in computational physics: Advances in research and applications* (Vol. 17,
563 pp. 173–265). Elsevier. doi: 10.1016/B978-0-12-460817-7.50009-4
564
565 Balsara, D. S., & Shu, C.-W. (2000). Monotonicity Preserving Weighted Essentially
566 Non-oscillatory Schemes with Increasingly High Order of Accuracy. *Journal of*
567 *Computational Physics*, 160(2), 405–452. doi: 10.1006/jcph.2000.6443
568
569 Bellon, G., & Stevens, B. (2012). Using the sensitivity of large-eddy simulations to
570 evaluate atmospheric boundary layer models. *Journal of the Atmospheric Sci-*
571 *ences*, 69(5), 1582–1601.
572
573 Bony, S. (2005). Marine boundary layer clouds at the heart of tropical cloud feed-
574 back uncertainties in climate models. *Geophysical Research Letters*, 32(20),
575 L20806. doi: 10.1029/2005GL023851
576
577 Bordoni, S., & Schneider, T. (2008). Monsoons as eddy-mediated regime transitions
578 of the tropical overturning circulation. *Nature Geoscience*, 1(8), 515–519. doi:
579 10.1038/ngeo248
580
581 Brient, F., & Schneider, T. (2016). Constraints on Climate Sensitivity from Space-
582 Based Measurements of Low-Cloud Reflection. *Journal of Climate*, 29(16),
583 5821–5835. doi: 10.1175/JCLI-D-15-0897.1
584
585 Brient, F., Schneider, T., Tan, Z., Bony, S., Qu, X., & Hall, A. (2016). Shallowness
586 of tropical low clouds as a predictor of climate models’ response to warming.
587 *Climate Dynamics*, 47(1-2), 433–449. doi: 10.1007/s00382-015-2846-0
588
589 Byun, D. W. (1990). On the Analytical Solutions of Flux-Profile Relationships for
590 the Atmospheric Surface Layer. *Journal of Applied Meteorology*, 29(7), 652–
591 657. doi: 10.1175/1520-0450(1990)029<0652:OTASOF>2.0.CO;2
592
593 Cess, R. D., Potter, G. L., Blanchet, J. P., Boer, G. J., Del Genio, A. D., Déqué,
594 M., ... Zhang, M.-H. (1990). Intercomparison and interpretation of climate
595 feedback processes in 19 atmospheric general circulation models. *Journal of*
596 *Geophysical Research*, 95(D10), 16601. doi: 10.1029/JD095iD10p16601
597
598 Cess, R. D., Zhang, M. H., Ingram, W. J., Potter, G. L., Alekseev, V., Barker,
599 H. W., ... Wetherald, R. T. (1996). Cloud feedback in atmospheric general
600 circulation models: An update. *Journal of Geophysical Research: Atmospheres*,
601 101(D8), 12791–12794. doi: 10.1029/96JD00822

- 594 Charney, J. G., Arakawa, A., Baker, D. J., Bolin, B., Dickinson, R. E., Goody,
595 R. M., . . . Wunsch, C. I. (1979). *Carbon dioxide and climate: a scientific*
596 *assessment*. National Academy of Sciences, Washington, DC.
- 597 Dal Gesso, S., & Neggers, R. (2018). Can we use single-column models for under-
598 standing the boundary layer cloud-climate feedback? *Journal of Advances in*
599 *Modeling Earth Systems*, *10*(2), 245–261.
- 600 Dipankar, A., Stevens, B., Heinze, R., Moseley, C., Zängl, G., Giorgetta, M., & Br-
601 dar, S. (2015). Large eddy simulation using the general circulation model icon.
602 *Journal of Advances in Modeling Earth Systems*, *7*(3), 963–986.
- 603 Dixit, V., Geoffroy, O., & Sherwood, S. C. (2018). Control of itcz width by low-level
604 radiative heating from upper-level clouds in aquaplanet simulations. *Geophysic-*
605 *cal Research Letters*, *45*(11), 5788–5797.
- 606 Dufresne, J.-L., & Bony, S. (2008). An Assessment of the Primary Sources of Spread
607 of Global Warming Estimates from Coupled Atmosphere-Ocean Models. *Jour-*
608 *nal of Climate*, *21*(19), 5135–5144. doi: 10.1175/2008JCLI2239.1
- 609 Durran, D. R. (1999). *Numerical Methods for Wave Equations in Geophysical Fluid*
610 *Dynamics* (Vol. 32). New York: Springer.
- 611 Frierson, D. M. W., Held, I. M., & Zurita-Gotor, P. (2006). A Gray-Radiation Aqua-
612 planet Moist GCM. Part I: Static Stability and Eddy Scale. *Journal of the At-*
613 *mospheric Sciences*, *63*(10), 2548–2566. doi: 10.1175/JAS3753.1
- 614 Frierson, D. M. W., Held, I. M., & Zurita-Gotor, P. (2007). A Gray-Radiation Aqua-
615 planet Moist GCM. Part II: Energy Transports in Altered Climates. *Journal of*
616 *the Atmospheric Sciences*, *64*(5), 1680–1693. doi: 10.1175/JAS3913.1
- 617 Grabowski, W. W. (1998). Toward cloud resolving modeling of large-scale tropical
618 circulations: A simple cloud microphysics parameterization. *Journal of the At-*
619 *mospheric Sciences*, *55*(21), 3283–3298. doi: 10.1175/1520-0469(1998)055<3283:
620 TCRMOL>2.0.CO;2
- 621 Hartmann, D. L., Gasparini, B., Berry, S. E., & Blossey, P. N. (2018). The life cycle
622 and net radiative effect of tropical anvil clouds. *Journal of Advances in Model-*
623 *ing Earth Systems*, *10*(12), 3012–3029.
- 624 Heinze, R., Dipankar, A., Henken, C. C., Moseley, C., Sourdeval, O., Trömel, S.,
625 . . . others (2017). Large-eddy simulations over germany using icon: A com-
626 prehensive evaluation. *Quarterly Journal of the Royal Meteorological Society*,
627 *143*(702), 69–100.
- 628 Kaul, C. M., Teixeira, J., & Suzuki, K. (2015). Sensitivities in Large-Eddy Sim-
629 ulations of Mixed-Phase Arctic Stratocumulus Clouds Using a Simple Mi-
630 crophysics Approach. *Monthly Weather Review*, *143*(11), 4393–4421. doi:
631 10.1175/MWR-D-14-00319.1
- 632 Knutti, R., Rugenstein, M. A. A., & Hegerl, G. C. (2017). Beyond equilibrium cli-
633 mate sensitivity. *Nature Geoscience*, *10*(10), 727–736. doi: 10.1038/ngeo3017
- 634 Lilly, D. K. (1962). On the numerical simulation of buoyant convection. *Tellus*,
635 *14*(2), 148–172. doi: 10.3402/tellusa.v14i2.9537
- 636 Matheou, G., Chung, D., Nuijens, L., Stevens, B., & Teixeira, J. (2011). On the Fi-
637 delity of Large-Eddy Simulation of Shallow Precipitating Cumulus Convection.
638 *Monthly Weather Review*, *139*(9), 2918–2939. doi: 10.1175/2011MWR3599.1
- 639 Merlis, T. M., & Schneider, T. (2011). Changes in Zonal Surface Temperature Gra-
640 dients and Walker Circulations in a Wide Range of Climates. *Journal of Cli-*
641 *mate*, *24*(17), 4757–4768. doi: 10.1175/2011JCLI4042.1
- 642 Neggers, R. A., Siebesma, A. P., & Heus, T. (2012). Continuous single-column
643 model evaluation at a permanent meteorological supersite. *Bulletin of the*
644 *American Meteorological Society*, *93*(9), 1389–1400.
- 645 O’Gorman, P. A., & Schneider, T. (2008). The Hydrological Cycle over a Wide
646 Range of Climates Simulated with an Idealized GCM. *Journal of Climate*,
647 *21*(15), 3815–3832. doi: 10.1175/2007JCLI2065.1
- 648 Pauluis, O. (2008). Thermodynamic Consistency of the Anelastic Approximation for

- 649 a Moist Atmosphere. *Journal of the Atmospheric Sciences*, 65(8), 2719–2729.
650 doi: 10.1175/2007JAS2475.1
- 651 Posselt, D. J., van den Heever, S. C., & Stephens, G. L. (2008). Trimodal cloudiness
652 and tropical stable layers in simulations of radiative convective equilibrium.
653 *Geophysical Research Letters*, 35(8), L08802. doi: 10.1029/2007GL033029
- 654 Pressel, K. G., Kaul, C. M., Schneider, T., Tan, Z., & Mishra, S. (2015). Large-
655 eddy simulation in an anelastic framework with closed water and entropy
656 balances. *Journal of Advances in Modeling Earth Systems*, 7(3), 1425–1456.
657 doi: 10.1002/2015MS000496
- 658 Pressel, K. G., Mishra, S., Schneider, T., Kaul, C. M., & Tan, Z. (2017). Nu-
659 merics and subgridscale modeling in large eddy simulations of stratocumulus
660 clouds. *Journal of Advances in Modeling Earth Systems*, 9(2), 1342–1365. doi:
661 10.1002/2016MS000778
- 662 Randall, D. A., & Cripe, D. G. (1999). Alternative methods for specification of
663 observed forcing in single-column models and cloud system models. *Jour-
664 nal of Geophysical Research: Atmospheres*, 104(D20), 24527–24545. doi:
665 10.1029/1999JD900765
- 666 Rauber, R. M., Stevens, B., Ochs III, H. T., Knight, C., Albrecht, B. A., Blyth, A.,
667 ... others (2007). Rain in shallow cumulus over the ocean: The rico campaign.
668 *Bulletin of the American Meteorological Society*, 88(12), 1912–1928.
- 669 Schalkwijk, J., Jonker, H. J. J., Siebesma, A. P., & Bosveld, F. C. (2015). A year-
670 long large-eddy simulation of the weather over Cabauw: An overview. *Mon.
671 Wea. Rev.*, 143, 828–844.
- 672 Schneider, T., Kaul, C. M., & Pressel, K. G. (2019). Possible climate transitions
673 from breakup of stratocumulus decks under greenhouse warming. *Nature
674 Geosci.*, 12, 163–167.
- 675 Schneider, T., Lan, S., Stuart, A., & Teixeira, J. (2017). Earth System Modeling 2.0:
676 A Blueprint for Models That Learn From Observations and Targeted High-
677 Resolution Simulations. *Geophysical Research Letters*, 44(24), 12,396–12,417.
678 doi: 10.1002/2017GL076101
- 679 Schneider, T., Teixeira, J., Bretherton, C. S., Brient, F., Pressel, K. G., Schär, C.,
680 & Siebesma, A. P. (2017). Climate goals and computing the future of clouds.
681 *Nature Climate Change*, 7(1), 3–5. doi: 10.1038/nclimate3190
- 682 Shu, C.-W., & Osher, S. (1988). Efficient implementation of essentially non-
683 oscillatory shock-capturing schemes. *Journal of Computational Physics*, 77(2),
684 439–471. doi: 10.1016/0021-9991(88)90177-5
- 685 Siebesma, A. P., Bretherton, C. S., Brown, A., Chlond, A., Cuxart, J., Duynkerke,
686 P. G., ... Stevens, D. E. (2003). A Large Eddy Simulation Intercomparison
687 Study of Shallow Cumulus Convection. *Journal of the Atmospheric Sciences*,
688 60(10), 1201–1219. doi: 10.1175/1520-0469(2003)60(1201:ALESIS)2.0.CO;2
- 689 Smagorinsky, J. (1963). General circulation experiments with the primitive equa-
690 tions. *Monthly Weather Review*, 91(3), 99–164. doi: 10.1175/1520-0493(1963)
691 091(0099:GCEWTP)2.3.CO;2
- 692 Sobel, A. H., & Bretherton, C. (2000). Modeling tropical precipitation in a single
693 column. *J. Climate*, 13, 4378–4392.
- 694 Sobel, A. H., Nilsson, J., & Polvani, L. M. (2001). The weak temperature gradi-
695 ent approximation and balanced tropical moisture waves. *J. Atmos. Sci.*, 58,
696 3650–3665.
- 697 Stein, T. H. M., Parker, D. J., Delanoë, J., Dixon, N. S., Hogan, R. J., Knip-
698 pertz, P., ... Marsham, J. H. (2011). The vertical cloud structure of
699 the West African monsoon: A 4 year climatology using CloudSat and
700 CALIPSO. *Journal of Geophysical Research: Atmospheres*, 116(D22). doi:
701 10.1029/2011JD016029
- 702 Stevens, B., Moeng, C.-H., Ackerman, A. S., Bretherton, C. S., Chlond, A., de
703 Roode, S., ... others (2005). Evaluation of large-eddy simulations via obser-

- 704 vations of nocturnal marine stratocumulus. *Monthly weather review*, 133(6),
 705 1443–1462.
- 706 Troen, I. B., & Mahrt, L. (1986). A simple model of the atmospheric boundary
 707 layer; sensitivity to surface evaporation. *Boundary-Layer Meteorology*, 37(1-2),
 708 129–148. doi: 10.1007/BF00122760
- 709 Van Laar, T. W., Schemann, V., & Neggers, R. A. (2019). Investigating the diurnal
 710 evolution of the cloud size distribution of continental cumulus convection using
 711 multiday les. *Journal of the Atmospheric Sciences*, 76(3), 729–747.
- 712 Vial, J., Dufresne, J.-L., & Bony, S. (2013). On the interpretation of inter-model
 713 spread in CMIP5 climate sensitivity estimates. *Climate Dynamics*, 41(11-12),
 714 3339–3362. doi: 10.1007/s00382-013-1725-9
- 715 Vial, J., Vogel, R., Bony, S., Stevens, B., Winker, D. M., Cai, X., ... Brogniez,
 716 H. (2019). A new look at the daily cycle of tradewind cumuli. *Journal of*
 717 *Advances in Modeling Earth Systems*.
- 718 Voigt, A., & Shaw, T. A. (2015). Circulation response to warming shaped by radia-
 719 tive changes of clouds and water vapour. *Nature Geoscience*, 8(2), 102.
- 720 Webb, M. J., Senior, C. A., Sexton, D. M. H., Ingram, W. J., Williams, K. D.,
 721 Ringer, M. A., ... Taylor, K. E. (2006). On the contribution of local feedback
 722 mechanisms to the range of climate sensitivity in two GCM ensembles. *Climate*
 723 *Dynamics*, 27(1), 17–38. doi: 10.1007/s00382-006-0111-2
- 724 Xiao, H., Gustafson Jr, W. I., & Wang, H. (2014). Impact of subgrid-scale radiative
 725 heating variability on the stratocumulus-to-trade cumulus transition in climate
 726 models. *Journal of Geophysical Research: Atmospheres*, 119(7), 4192–4203.